Mechanical Performance of Bio-Inspired Gyroid and Primitive Concrete Structures under Combined Compression and Torsion Loads

Fu, Hao; Huang, Junhui; Kaewunruen, Sakdirat

DOI:
10.1016/j.engstruct.2023.116429

Document Version
Publisher's PDF, also known as Version of record

Citation for published version (Harvard):
Fu, H, Huang, J & Kaewunruen, S 2023, 'Mechanical Performance of Bio-Inspired Gyroid and Primitive Concrete Structures under Combined Compression and Torsion Loads: A Discrete Element Method Study', *Engineering Structures*, vol. 291, 116429. https://doi.org/10.1016/j.engstruct.2023.116429

Engineering Structures 291 (2023) 116429

Contents lists available at ScienceDirect

Engineering Structures

journal homepage: www.elsevier.com/locate/engstruct

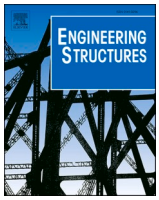

Mechanical performance of Bio-Inspired Gyroid and Primitive concrete structures under combined compression and torsion Loads: A discrete element method study

Hao Fu [a], Junhui Huang [a], Sakdirat Kaewunruen [a,*]

[a] Laboratory for Track Engineering and Operations for Future Uncertainties (TOFU Lab), Department of Civil Engineering, School of Engineering, The University of Birmingham, Edgbaston, B15 2TT Birming-ham, United Kingdom

ARTICLE INFO

Keywords:
Discrete element method
Typical triply periodic minimal surface
Compression
Torsion
Crack

ABSTRACT

Bioinspired lightweight Primitive and Gyroid structures are two well-known TPMS (triply periodic minimal surface) cellular structures. These structures have been shown to possess high specific strength and energy absorption capacity, and thus hold great promise for a range of prefabricated civil engineering applications. As a result, concrete cellular TPMS structures have garnered the attention of researchers. However, prior to this study, no investigation has been carried out on the mechanical properties and failure patterns of concrete Primitive and Gyroid structures under coupled compressive and torsional loads. This lack of knowledge on the behaviour of these structures can lead to safety concerns in construction projects. To better understand the mechanical behaviour of Primitive and Gyroid structures under combined compression and torsion, the discrete element method (DEM) is adopted to simulate the TPMS structures. Both linear contact and nonlinear softbond contact models are utilized to simulate the brittle mechanical behaviour of concrete material. After validating the DEM parameters using published experimental data, the DEM models are subjected to coupled compressive and torsional loads to study their compressive and torsional bearing capacity and cracking patterns. The results indicate that the Primitive based structures outperform the Gyroid based structures in terms of both compressive and torsional resistance. The study is the world's first to reveal that a compressive load enhances the ultimate torsional bearing capacity of TPMS structures, but a torsional load reduces their compressive bearing capacity. Additionally, the loading conditions have little impact on the cracking patterns of the four TPMS structures.

1. Introduction

In recent decades, the development of additive manufacturing technologies, also known as 3D printing, and relevant materials has advanced rapidly. Compared to traditional subtractive technologies, 3D printing offers greater material utilization and the capability to fabricate specimens with intricate shapes [1,2]. The evolution of 3D technology and materials has led to an increased investigation of complex macro-porous lightweight structures and micro-porous materials [3,4]. Cellular structures, due to their periodic structural form and favourable mechanical behaviour, have procured substantial interest among lightweight structures. Cellular structures have been applied in a variety of engineering fields, including biological engineering [5,6], aerospace [7,8], and robotics [9], due to their high specific strength [10–12], good stiffness [13] and excellent energy absorption capacity[14,15]. The periodic unit cell arrangement of cellular structures results in homogeneous and designable mechanical properties in all directions [16].

The Triply Periodic Minimal Surface (TPMS) structures have emerged as a promising type of cellular structure in the last two decades, due to their similarity to structures found in nature [17–19]. These structures possess three-dimensional interconnected pores and exhibit symmetry or antisymmetry. Numerous studies have explored the mechanical properties of TPMS-based structures, including stiffness, modulus, bulk modulus, compressive strength, energy absorption, and cracking patterns [20–39]. The results showed that TPMS structures outperform conventional lattice. Even compared to the recently developed spinodal lattice [40] and plate lattice [41], TPMS structures exhibit comparable static mechanical properties. However, it should be noted that the majority of research on TPMS-based structures has focused on elastic–plastic materials, such as metals, alloys, and polymers, for use in

* Corresponding author.
E-mail address: S.Kaewunruen@bham.ac.uk (S. Kaewunruen).

https://doi.org/10.1016/j.engstruct.2023.116429
Received 17 February 2023; Received in revised form 5 May 2023; Accepted 3 June 2023
Available online 8 June 2023

tissue engineering and robotics. These materials are not suitable for construction applications, which often require small deformations under working loads. Concrete, being a cheap and widely used material with good mechanical properties and chemical resistance, is a more common choice for construction purposes due to its large-scale consumption.

From a civil engineering standpoint, building and construction materials must satisfy the demands for safety, adaptability, and durability of structures. Additionally, materials must possess cost-effectiveness and high-value mechanical and chemical properties to balance the engineering cost and performance. Concrete materials are widely adopted in civil engineering and construction for their high stiffness, good hardness, excellent compressive strength, and low cost. In recent years, researchers have explored the use of smart macro-porous concrete structures, such as honeycomb concrete walls [42] and honeycomb cellular beams [43]. The advancement of 3D concrete printing (3DCP) technologies and materials has garnered significant attention in the last two decades [44–46]. Compared to traditional concrete production methods, 3DCP enables the fabrication of structures with complex porous shapes for prefabricated architectures [15,47–52]. To incorporate TPMS structures into civil engineering, some researchers have begun investigating macro TPMS structures manufactured from materials suitable for civil engineering applications [15,49,53–58]. In civil engineering, TPMS structures have been identified as potential solutions for load-bearing structures such as bridges and buildings. Their superior mechanical properties and energy-absorbing abilities make them suitable for use in energy-absorbing systems, such as seismic dampers and shock absorbers. TPMS structures also have the potential to be used as effective noise barriers, as laboratory tests have demonstrated their ability to reduce sound transmission and improve acoustics. In addition to their practical applications, TPMS structures also offer decorative potential in architectural designs due to their intricate and repeating patterns. This can add a unique and visually appealing aspect to structures. Furthermore, TPMS structures' lightweight and efficient structure make them ideal for use in light-weight construction. In conclusion, the promising potential applications of TPMS structures in civil engineering are due to their superior mechanical properties, energy-absorbing capabilities, acoustics performance, decorative potential, and lightweight efficiency.

In previous literature, the mechanical behaviour of TPMS-based concrete structures under compressive loads has been studied. However, despite the demonstrated high energy absorption capacity and specific strength of TPMS-based structures under uniaxial loads, the response of these structures under combined compressive and torsional loads has yet to be explored. In practical civil engineering applications, many structural components are subjected to combined stress. The bearing capacity of a structure under composite forces is significantly different from that under uniaxial loads, and it is unclear how the bearing capacity and failure modes of TPMS-based structures would be affected under such loads. The limited understanding of TPMS structures under combined compression and torsion hinders their widespread use. To address this knowledge gap, this study aims to investigate the mechanical behaviour of various TPMS-based structures under different levels of combined compressive and torsional loads.

In this study, we employ discrete element methods (DEM) to investigate the mechanical behaviour of TPMS-based structures, made of brittle concrete material, subjected to combined compressive and torsional loads. The ball elements are utilized to simulate the concrete TPMS structures, and a novel simulation approach has been proposed, based on DEM, to model concrete structures with complex geometries. The linear contact model (LCM) and nonlinear softbond model (SBM) are employed to transfer the contact forces and moments. The model is able to demonstrate the crack propagation in the TPMS-based structures. To calibrate the DEM parameters, two models are initially constructed, based on Gyroid and Primitive structures, using experimental data from [53]. Then, the main and secondary skeletal Gyroid and Primitive structures are built using the validated parameters and examined for their performance under combined compressive and torsional loads with varying intensities. For the first time, the bearing capacity of the concrete Primitive and Gyroid structures is compared under different load types. The impact of torsion on the compressive bearing capacity and the impact of compression on the torsional bearing capacity of the concrete Primitive and Gyroid structures are also studied. Lastly, the cracking patterns of the concrete Primitive and Gyroid structures are investigated.

2. Numerical simulation methods

2.1. Mathematical equation of TPMSs

The Gyroid and Primitive surfaces are widely recognized as two attractive Triply Periodic Minimal Surfaces (TPMSs) in prior research. Their mechanical and thermophysical properties have been extensively studied using both experimental methods and Finite Element Methods (FEMs). This study investigates the performance of structures with concrete material properties and the two TPMSs' topologies under coupled compression and torsion. Eq. (1) and Eq. (2) present the mathematical approximations of the Gyroid and Primitive surfaces. Fig. 1 depicts these two TPMSs, plotted using triangle meshes. It is important to note that, in order to construct the skeletal Primitive and Gyroid structures, the perfect continuous curved TPMSs have been simplified into polygonal surfaces using the method described in [19].

$$\phi_{\text{Gyroid}} = \sin(\frac{2\pi x}{l})\cos(\frac{2\pi y}{l}) + \sin(\frac{2\pi y}{l})\cos(\frac{2\pi z}{l}) + \sin(\frac{2\pi z}{l})\cos(\frac{2\pi x}{l}) = C \tag{1}$$

$$\phi_{\text{Primitive}} = \cos(\frac{2\pi x}{l}) + \cos(\frac{2\pi y}{l}) + \cos(\frac{2\pi z}{l}) = C \tag{2}$$

2.2. Geometric model

Initially, the software MATLAB is employed to create the STL files of the Gyroid and Primitive surfaces. Subsequently, the meshed TPMSs are imported into Geomagic Studio for constructing solid TPMS structures. The skeletal TPMS structures are formed by solidifying the two non-overlapping regions ($\Phi_{TPMS} \geq C$ and $\Phi_{TPMS} \leq C$). These two classes of TPMS structures are classified as the main skeletal type and the secondary skeletal type determined by the mathematical inequality. The main skeletal TPMS (MS-TPMS) type corresponds to the inequality $\Phi_{TPMS} \geq C$, while the secondary skeletal TPMS (SS-TPMS) type corresponds to the inequality $\Phi_{TPMS} \leq C$. As the TPMS divides the space into two regions with equivalent relative volumes (50%), all skeletal TPMS structures possess the same relative density (0.5). Fig. 2 illustrates the unit cells of the main skeletal and secondary skeletal types of the Gyroid and Primitive structures.

2.3. DEM models

In this section, the discrete element simulation software, PFC 3D, is utilized to fabricate porous TPMS structures subjected to combined compressive and torsional loads. The TPMS structures are represented using breakable clusters consisting of interacting ball elements, and both the linear contact model and the soft bonded model are employed. The model parameters are calibrated with experimental data prior to analyzing the mechanical responses of the TPMS structures under composite loading conditions. The compressive loads are imposed using rigid wall elements, while the torsional forces are modelled via rotational speed. The study aims to determine the ultimate compressive and torsional capacities, as well as the cracking patterns, of the TPMS structures.

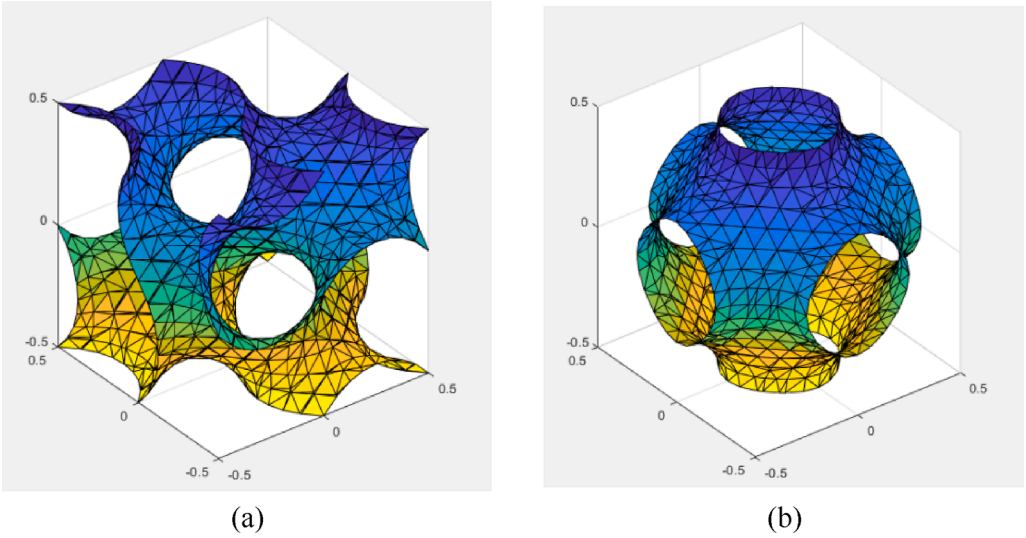

Fig. 1. The simplified polygonal representations of the two representative TPMSs: (a) Gyroid surface and (b) Primitive surface.

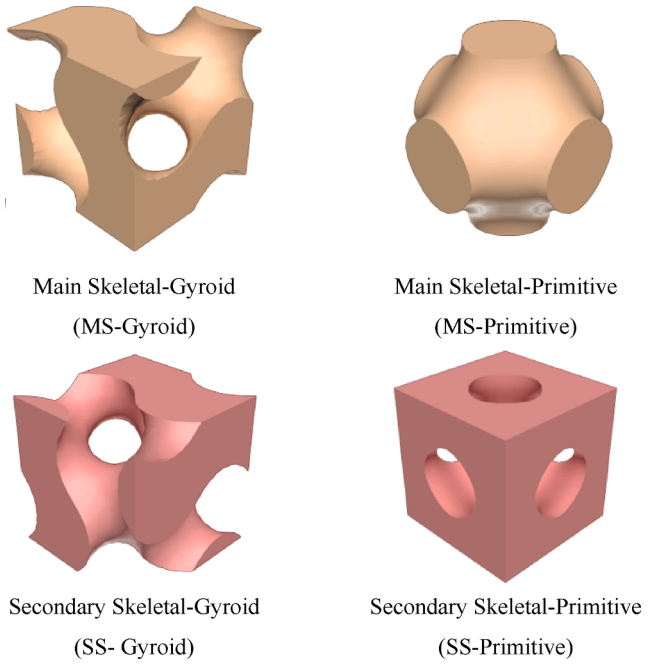

Fig. 2. Unit cells with 0.5 relative density of the main skeletal and secondary skeletal TPMS structures of the Gyroid and Primitive surfaces.

2.3.1. Generation of TPMS unit

This section details the procedure for simulating the unit cells of porous TPMS structures using the discrete element software, PFC 3D. Firstly, the STL files of the TPMS units are scaled and imported into PFC 3D to generate the shapes of all TPMS units. Each TPMS unit has a uniform size (50 mm × 50 mm × 50 mm). The confinement of the cluster of TPMS units is established through the use of rigid Wall elements, as depicted in Fig. 3, which are composed of multiple triangular facets. Subsequently, Ball elements of radii ranging from 2 mm to 3 mm are generated and placed within the designated area, allowing for overlaps. The Wall elements are activated on both sides, while the Ball elements are assigned the material properties of concrete. The Ball elements are then subjected to linear contact models, and the model is solved until the average unbalanced force ratio of all Ball elements reaches 0.0001, thereby ensuring their uniform distribution. The unit cells of MS-Gyroid, SS-Gyroid, MS-Primitive and SS-Primitive structures are modelled with 1874, 1987, 2035 and 2135 Ball elements, respectively. To further consolidate the TPMS units as clusters, a soft bonded model (SBM) is implemented to make the contact elements breakable. The resulting breakable TPMS unit clusters are exported as Bricks for subsequent modelling.

2.3.2. Contact models

The contact model formulates a relationship between the generalized internal force and the relative motion at the point of contact through a force–displacement law. This relationship results in the internal force and moment (F and M) acting upon the two bodies in question, with equal and opposing effects, as depicted in Fig. 4.

The linear contact models (LCMs) are employed to simulate the Wall-Ball contacts and impose compressive and torsional loads through the translational and rotational movements of the Walls. The linear contacts are activated when the gap between the Ball elements and the Wall elements is equal to or less than zero. The force–displacement relationship is then governed by equations Eq. (3) to (8). The k indicates stiffness. The β represents the critical damping ratio. The F signifies the contact force, comprised of linear force (F^l) and the dashpot force(F^d). The δ is the overlap between the two contacted bodies. The μ is the frictional coefficient. The $\Delta\delta$ is the relative displacement increment at the contact during a timestep. The subscripts n and s indicate the normal and shear directions, respectively. An LCM incorporates both a linear spring and a dashpot, enabling it to simulate both linear elastic (compression only) and viscous behaviour. The linear spring and dashpot act over a minute area, transmitting force but not a moment.

$$F_n^l = k_n \delta_n \tag{3}$$

$$F_{s^*}^l = \left(F_s^l\right)_0 - k_s \Delta\delta_s \tag{4}$$

$$F_s^l = \begin{cases} F_{s^*}^l, if F_{s^*}^l \le \mu F_n^l \\ \mu F_n^l, if F_{s^*}^l > \mu F_n^l \end{cases} \tag{5}$$

$$F_s^d = (2\beta_s \sqrt{m_c k_s})\dot{\delta}_s \tag{6}$$

$$F_n^d = \left(2\beta_n \sqrt{m_c k_n}\right)\dot{\delta}_n \tag{7}$$

$$m_c = \frac{m_1 m_2}{m_1 + m_2} \tag{8}$$

The soft-bond method (SBM) is adopted to simulate the breakable bonded contacts between Ball elements. The SBM is a uniformly

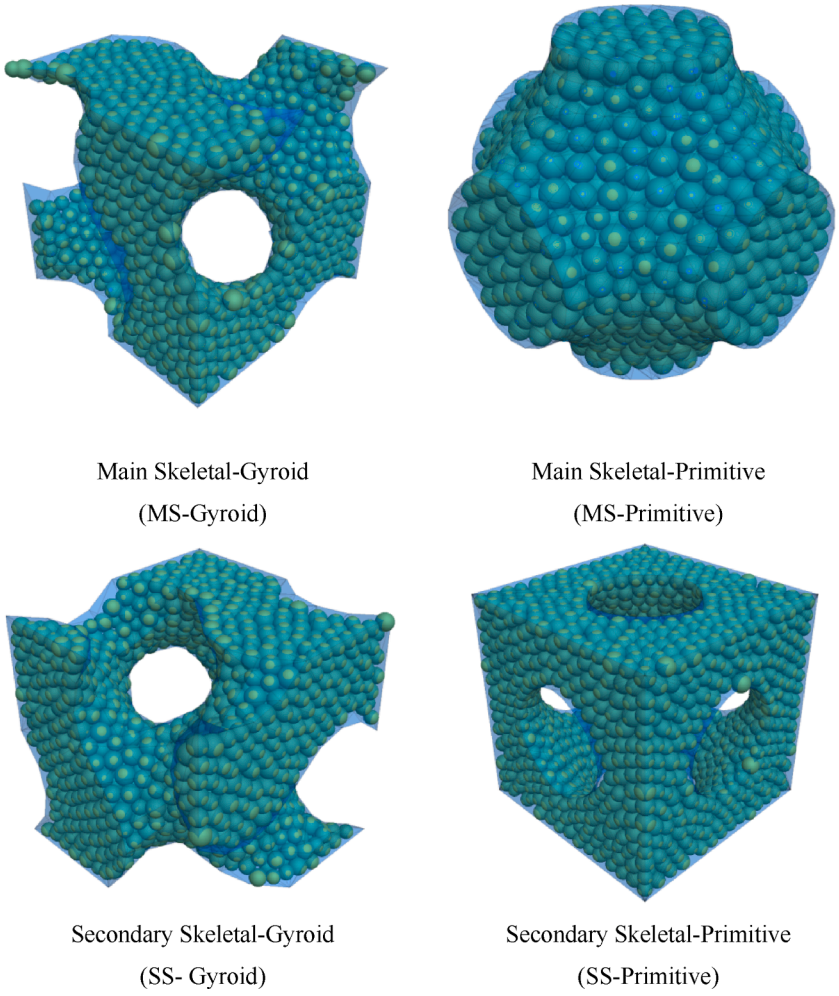

Fig. 3. DEM models of unit cells with 0.5 relative density of the main skeletal and secondary skeletal TPMS structures of the Gyroid and Primitive surfaces.

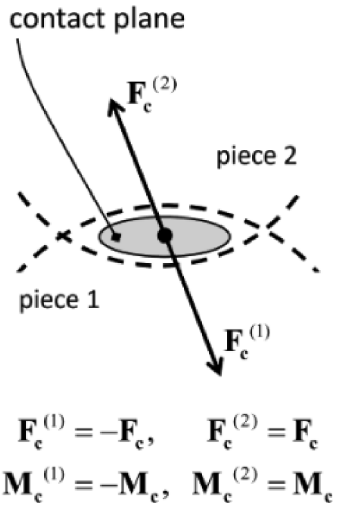

Fig. 4. An illustration of an active contact element between two ball elements, showing the internal forces and moments.

distributed elastic spring system with constant stiffness in both normal and shear directions. It resembles the Parallel Bond Model (PBM) in its behaviour. However, the SBM can undergo softening if the bond reaches a threshold value. When the bond is active, the force and moment can be related to the maximum normal and shear stresses at the bond periphery. If these stresses exceed the bond strength, the bond may enter into a softening regime according to specific failure criteria. Upon failure, the behaviour returns to the unbonded formulation. The force–displacement laws for active soft-bonded contact can be expressed as Eq. (9) to (15). The SBM model can transfer both the contact force and moment. The contact force is composed of the linear force and dash force. The dash force is updated the same as it is in the LCM model as presented in Eq. (6) and (7). The linear contact forces in the normal direction and shear direction are updated using the formulas Eq. (9) and (10). The contact moment is the combination of the twisting moment (M_t) and bending moment (M_b). In these equations, $\Delta\delta_s$ and $\Delta\delta_n$ are the relative displacement increment in the shear and normal directions. The $\Delta\theta_t$ and $\Delta\theta_b$ are the relative twist-rotation increment and relative bend-rotation increment. A and J are the cross-sectional area of the contact plane and the polar moment of inertia of the parallel bond cross-section. The R is the radius of the contact plane. The rheological components of the LCM and the SBM are presented in Fig. 5. For the DEM models, several numerical parameters should be set to activate the contact elements.

$$F_n = \max(F_n + k_n A \Delta\delta_n, 0) \tag{9}$$

$$F_s = F_s - k_s A \Delta\delta_s \tag{10}$$

$$M_t = M_t - k_s J \Delta\theta_t \tag{11}$$

$$M_b = M_b - k_n I \Delta\theta_b \tag{12}$$

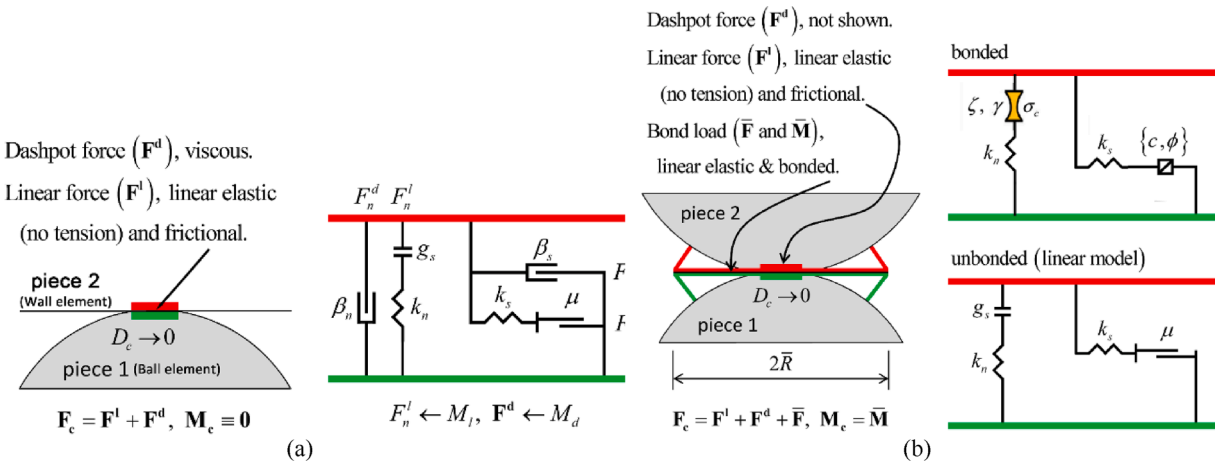

Fig. 5. The rheological components of (a) Linear contact model for the contacts between Wall and Ball elements and (b) Soft-bond contact model for the contacts between Ball and Ball elements.

$$A = \pi R^2 \tag{13}$$

$$I = \frac{1}{4}\pi R^4 \tag{14}$$

$$J = \frac{1}{2}\pi R^4 \tag{15}$$

2.3.3. Model validation

In order to validate the Discrete Element Method (DEM) models, the construction of two models are undertaken: a secondary skeletal Primitive model and a main skeletal Gyroid model, each with a $2 \times 2 \times 2$ unit cell arrangement, in accordance with the axially loaded tests outlined in [53]. The size of the Triply Periodic Minimal Surface (TPMS) structures is maintained at 10 cm $\times$ 10 cm $\times$ 10 cm, in line with the specifications detailed in [53]. The bricks constituting the two TPMS structures are

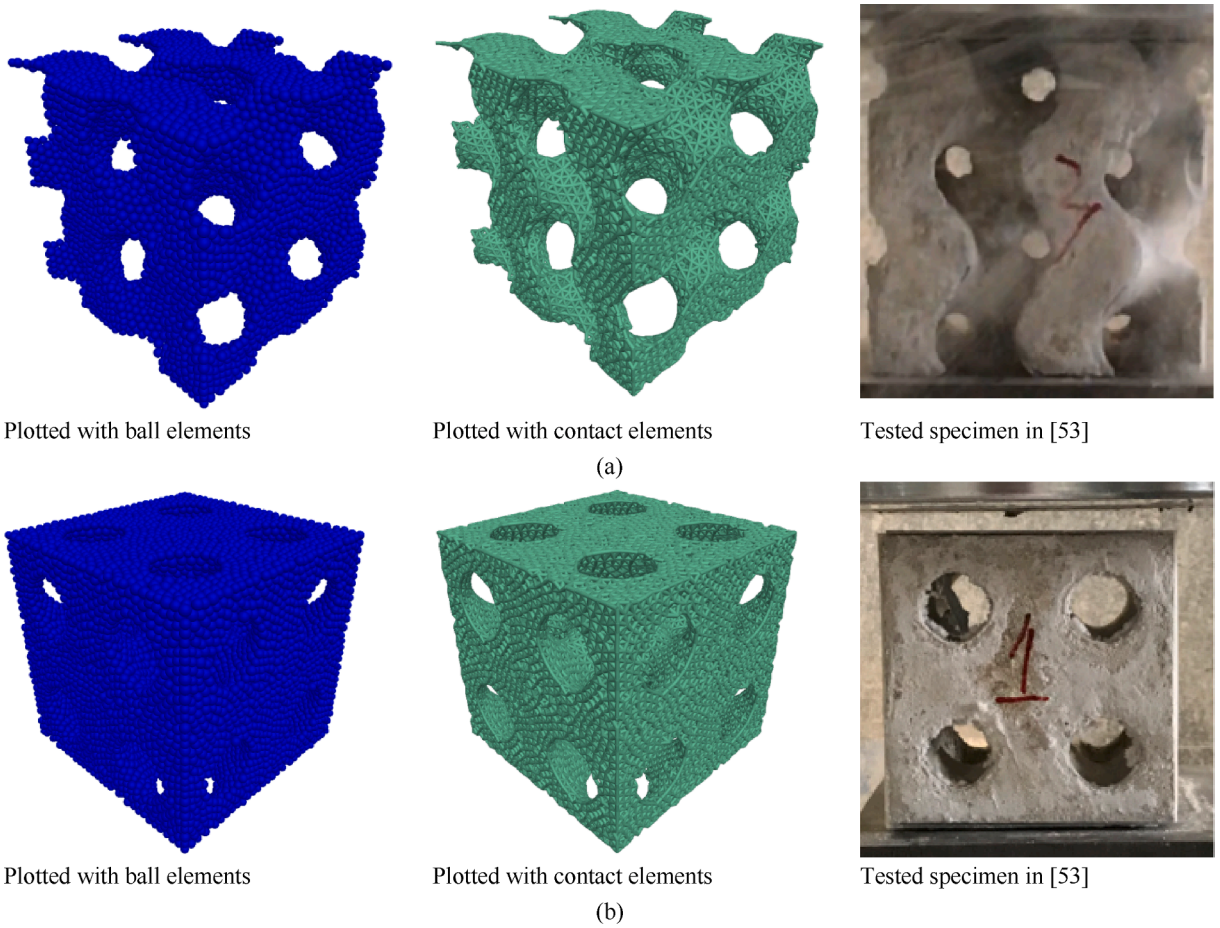

Fig. 6. The validation of the discrete element method (DEM) models, which employ Ball elements and contact elements, against the tested specimens described in [53]. The figure depicts (a) Main Skeletal-Gyroid (MS-Gyroid) structure and (b) Secondary Skeletal-Primitive (SS-Primitive) structure.

replicated in three dimensions and bonded together through the use of the SBM method. The DEM models are then solved until they achieve an equilibrium state, thereby relieving any internal stress. The linear contact is updated using an absolute mode, while the soft-bond model is updated incrementally. The DEM models created for validation purposes and the concrete specimens tested, as described in [53] are presented in Fig. 6.

Following the concrete properties outlined in [53] and the concrete discrete element method (DEM) models described in [59,60], the micro-parameters for the ball and wall elements in the DEM are set as listed in Table 1. The parameters for different contact models are listed in Table 2. The ultimate tensile strength is selected as 10% of the compressive strength of the concrete cube, which is determined to be 26.3 MPa in [53]. The tensile strength of the SBM contacts was set using a Gaussian distribution with a mean of 2.63 MPa and a standard deviation of 0.37 MPa. The critical damping ratios are set following the literature [61]. The normal normal-to-shear stiffness ratio is calculated by the Poisson's ratio using the method in [62]. The remaining multiplier parameters, including the radius multiplier and moment-contribution factor, are set to their default values. The top and bottom walls are subjected to loading rates of 2 mm/min and −2 mm/min, which applies a displacement load on the structures equivalent to the stress rate observed in experimental tests. The axial deformation of the simulated specimen is recorded by measuring the total displacement of the top and bottom wall elements. The axial load is calculated by aggregating the contact forces in the Z-direction of the Ball-Facet contacts between the top wall and the breakable TPMS cluster.

The load–displacement curves of the MS-Gyroid and SS-Primitive structures obtained from the Discrete Element Method (DEM) simulation and experiments under similar loading conditions are compared in Fig. 7. The forces and displacements from the experiments are derived from the stress versus strain data, calculated using the structural cross-sectional area and the height of the specimens (the experimental results are represented by black lines and the outcomes from the DEM analysis are depicted by red lines). All the specimens have the same height (10 cm). The effective cross-sectional area of the TPMS structures is half that of the cubic block (50 cm^2) due to the relative density of all the TPMS structures investigated in the study being 0.5 [53]. In general, the load–displacement curves obtained through the DEM numerical simulation of the two cellular structures show similar behaviour compared to the experimental results. Both the DEM and experimental results indicate that the load–displacement curves reach their peak load values at approximately 1 to 2 mm deformation. The ultimate load difference between the experimental results and the DEM results is 1.26% for the MS-Gyroid structure and 3.02% for the SS-Primitive structure. The correlation coefficient of the numerical and experimental load–displacement curve of the MS-Gyroid structure before reaching its the peak load is 0.958 (for displacement values between 0 mm and 2 mm), while after reaching the maximum load, the correlation coefficient is 0.972 (for displacement values between 2 mm and 6.5 mm). For the SS-Primitive structure, the load–displacement curve of exhibits a correlation coefficient of 0.944 prior to reaching its maximum load, over a displacement range of 0 mm to 1.2 mm, and a correlation coefficient of 0.949 after reaching the maximum load, over a displacement range of 1.2 mm to 6.5 mm. Throughout the entire displacement range (0 mm to 6.5 mm), the correlation coefficients of the MS-Gyroid structure and the SS-Gyroid structure are 0.951 and 0.753, respectively. These results indicate a strong correlation between the experimental and simulated data, which suggests that the model is reliable.

Table 1
The parameters for the Ball and Wall elements.

Parameters	Ball elements	Wall elements
Density (kg/m^3)	2100	–
Effective modulus (N/m^2)	1e10	2e10
Friction coefficient	0.6	0.6
Normal to shear stiffness,k_n/k_s	2.4	2.4

Table 2
The parameters for the LCM and SBM contact models.

Parameters	LCM	SBM
Effective modulus (N/m^2)	4e9	2e9
Friction coefficient	0.6	0.6
Normal to shear stiffness,k_n/k_s	2.4	2.4
Friction coefficient	0.6	0.6
Critical damping ratio	0.5	0.5
Poisson's ratio	0.2	0.2
Reference gap, gr (m)	0	0
Tensile strength, (N/m^2)	–	$2.63 \pm 3 \times 0.37$
Shear strength, (N/m^2)	–	auto updated
Update mode	absolute	increment
Softening factor, ξ	–	2.5
Softening tensile strength factor, γ	–	0.7
Friction angle, degrees	–	35

Fig. 8 compares the cracking areas of the MS-Gyroid and SS-Primitive structures. The DEM models at a displacement of 6.5 mm are drawn using Contact elements and Ball elements. The DEM models plotted using Ball elements cracked into several pieces, each depicted in different colours. The presence of different colors in adjacent ball units signifies a fracture of the bonding between them, indicating the occurrence of cracking. The red markers indicate the areas where cracking occurred, corresponding to both the experimental test from [53] and DEM simulation. The DEM model, which utilizes contact elements, illustrates the distribution of compressive and tensile contact elements within the model. Areas with a high number of tensile contacts are prone to cracking, as concrete is brittle in tension. It can be observed that the DEM models have similar cracking areas to the experimental results under compressive loads, implying that the DEM models, with proper material properties, can predict the strength and cracking patterns of TPMS-based structures.

2.3.4. Coupled load simulation procedures

In this section, the procedures for modelling the behaviours of the Gyroid and Primitive structures under combined compression and torsion loads are introduced. A total of four TPMS structures are studied in this paper, including the Main Skeletal-Gyroid, Secondary Skeletal-Gyroid, Main Skeletal-Primitive, and Secondary Skeletal-Primitive structures.

To start, the unit bricks of the four TPMS structures generated using the method in section 2.3.1 are replicated and assembled in a $2 \times 2 \times 2$ arrangement. Then, the bricks are bonded using SBM with the previously validated material properties. The inner contact forces and moments are then released by solving the models until the ratio-average (the average unbalanced force ratio of the Ball elements) reaches 0.0001.

Subsequently, two rigid caps (two rigid Wall elements), each with ten triangular facets, are generated at the top and bottom of the TPMS structures. As shown in Fig. 9, the compressive load is applied by attributing opposite motion velocities to the top and bottom Walls. The torsional load is applied by imparting a spin speed to the top and bottom Wall elements. The compressive load is recorded by summing the contact forces in the z-direction of all Ball-Facet contact elements. The torsional load is measured by recording the contact moments of the top Wall in the z-direction. For the MS-Primitive structure, unbreakable bonded contact elements are used to bond the ball elements near the top and bottom walls to the wall elements.

3. Results and discussion

In this section, the comparison of the mechanical behaviours of Main Skeletal and Secondary Solid Type TPMS cellular structures with Gyroid

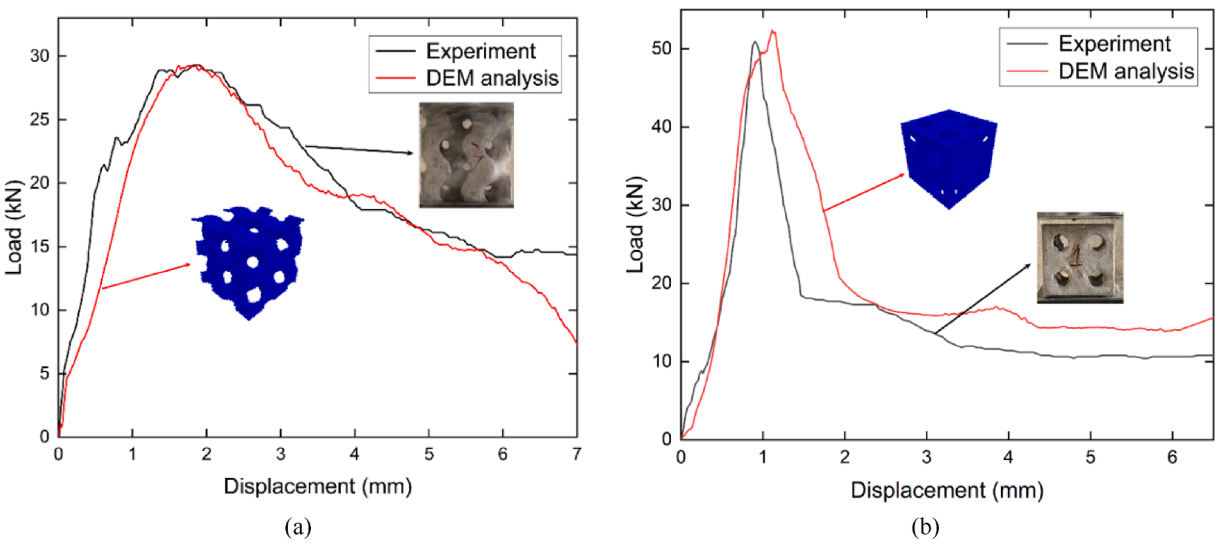

Fig. 7. Comparison of experimental tests and DEM simulation of (a) Main Skeletal-Gyroid structure and (b) Secondary Skeletal-Primitive structure under only compressive load.

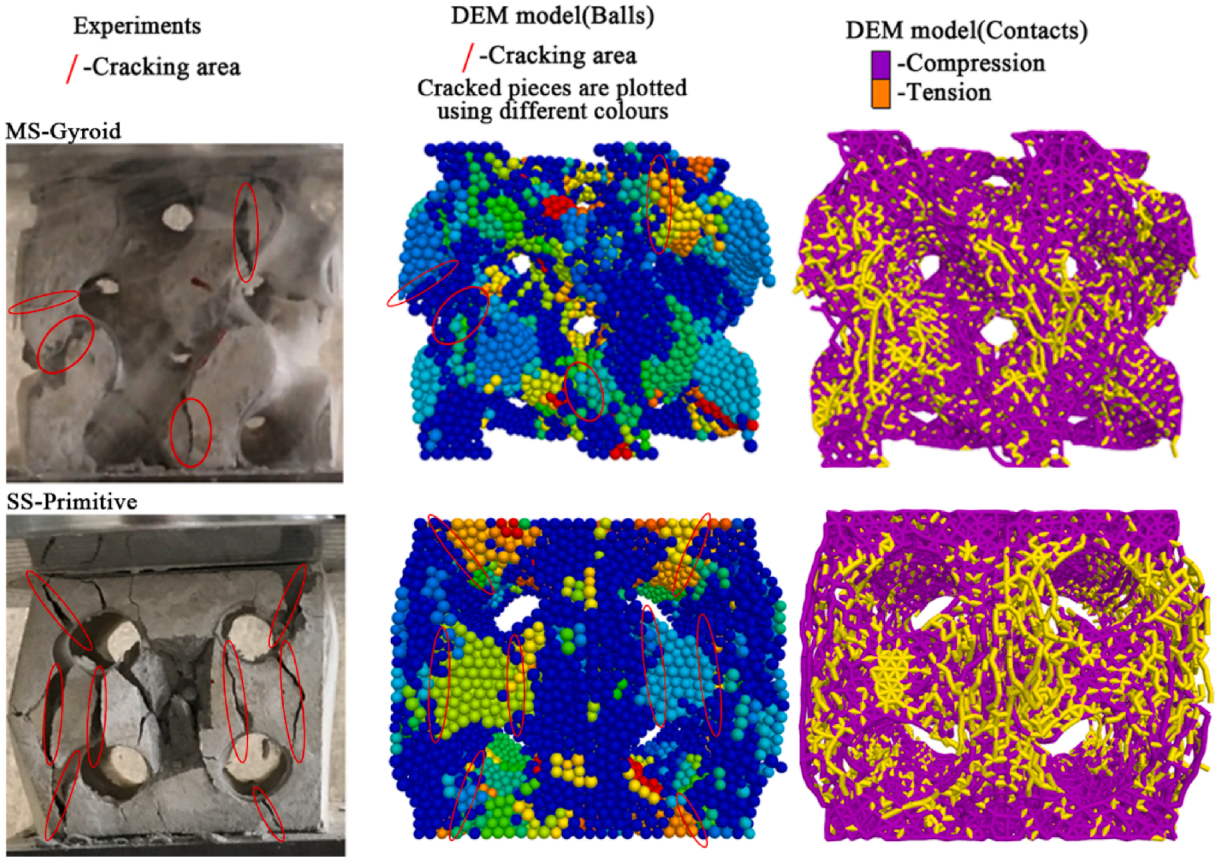

Fig. 8. Comparison of cracking areas, marked in red lines, between DEM simulation and experimental tests for Main Skeletal-Gyroid structure and Secondary Skeletal-Primitive structure under compressive loads only. The DEM models are plotted using both Contact elements and Ball elements. The cracked pieces of DEM models with Ball elements are drawn with different colours.

and Primitive surfaces is presented based on the results of Discrete Element Method (DEM) simulation. The focus of the study is on the comparison of the load-bearing capacity and cracking patterns of the structures under three different loading conditions: compression only, torsion only, and coupled torsion and compression.

3.1. Behaviours of TPMS structures under only compression

Fig. 10 compares the compressive load–displacement curves of MS-Gyroid, SS-Gyroid, MS-Primitive and SS-Primitive structures with the same unit cell arrangement ($2 \times 2 \times 2$) under compression only. It can be observed that the Primitive-based structures exhibit a much higher ultimate compressive strength compared to the Gyroid-based structures.

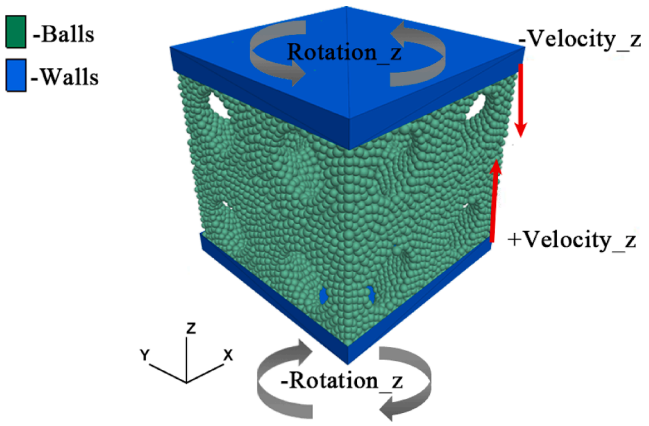

Fig. 9. DEM modelling of TPMS based structures under coupled compression and torsion loads. The compressive load is applied by the motion of the Wall Elements. The torsional load is applied by the rotation of the Wall elements.

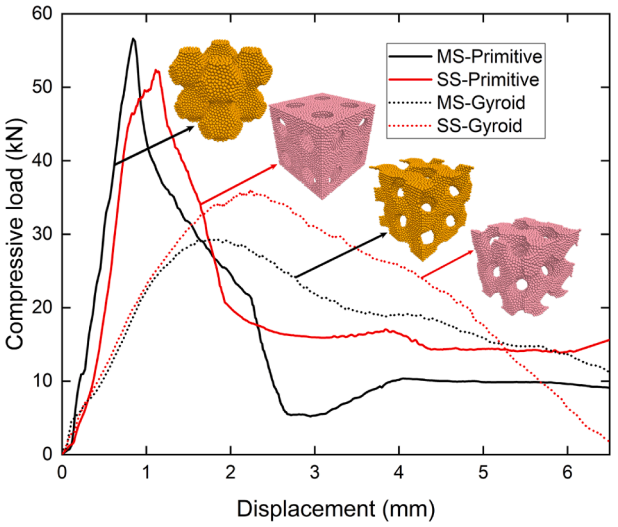

Fig. 10. The compressive load–displacement curves of the Gyroid and Primitive based structures under only compression.

The ultimate compressive loads for MS-Primitive, SS-Primitive, MS-Gyroid, and SS-Gyroid structures are 56.6 kN, 52.4 kN, 29.3 kN and 35.9 kN, respectively. The difference in compressive strength between MS-Primitive and SS-Primitive structures is 7.5 %, while the difference between the Gyroid based structures is 18.6%. This disparity can be attributed to the fact that the main skeletal TPMS based structures share the same 1/8 unit cell structures as the secondary skeletal TPMS based structures, with a phase difference of only a half unit cell size in each axial direction. Because the nodal mathematical approximations satisfy $\Phi_{TPMS}(x+\pi,y+\pi,z+\pi) = -\Phi_{TPMS}(x,y,z)$, the area $\Phi_{TPMS}(x,y,z) \geq 0$ equals $\Phi_{TPMS}(x+\pi,y+\pi,z+\pi) \leq 0$. As the number of unit cells in each axial direction increases, the compressive strengths of the main Skeletal TPMS and Secondary Skeletal TPMS tend to converge.

Fig. 11 shows the TPMS models, represented as ball elements with fractures and contact elements, after failure under compression only. The red disks indicate the locations where the bonded contacts broke. It can be seen that the Primitive-based structures undergo cracking mainly along the vertical direction and shattered into several large pieces, while the Gyroid structures break into numerous small fragments.

3.2. Behaviours of TPMS structures under only torsion

In Fig. 12, the relationship between torsional load and the rotation angle of the top wall for different TPMS structure DEM simulations under torsional loading only are presented. Given that spin speed has an impact on the ultimate torsional load, the simulations are conducted at different spin speeds ranging from 5°/min to 30°/min with increments of 5°. Results demonstrate that all TPMS structures demonstrate higher ultimate torsional loads as the loading rate increases. The ultimate torsional loads of MS-Primitive, SS-Primitive, MS-Gyroid, and SS-Gyroid at a spin rate of 30°/min are 1.34, 1.62, 1.72, and 1.28 times the ultimate torsional loads at a spin rate of 5°/min, respectively. The MS-Primitive, SS-Primitive and SS-Gyroid structures exhibit three stages, as shown in Fig. 12 (a) and (b), when subjected to torsional loading. In the first stage, torsional load increases as the rotation angle increases. In the second stage, the growth rate of the torsional load slows down, and there may even be a partial decrease due to the occurrence of cracking. However, overall, the torsional load still increases slowly during this stage. After reaching the ultimate load, in the third stage, the torsional bearing capacity of the TPMS structures gradually decreases, and even small torsional loads can cause significant twisting angles. On the other hand, the torsional load-rotation angle curves of the MS-Gyroid structures show only two stages, where the torsional load increases to the

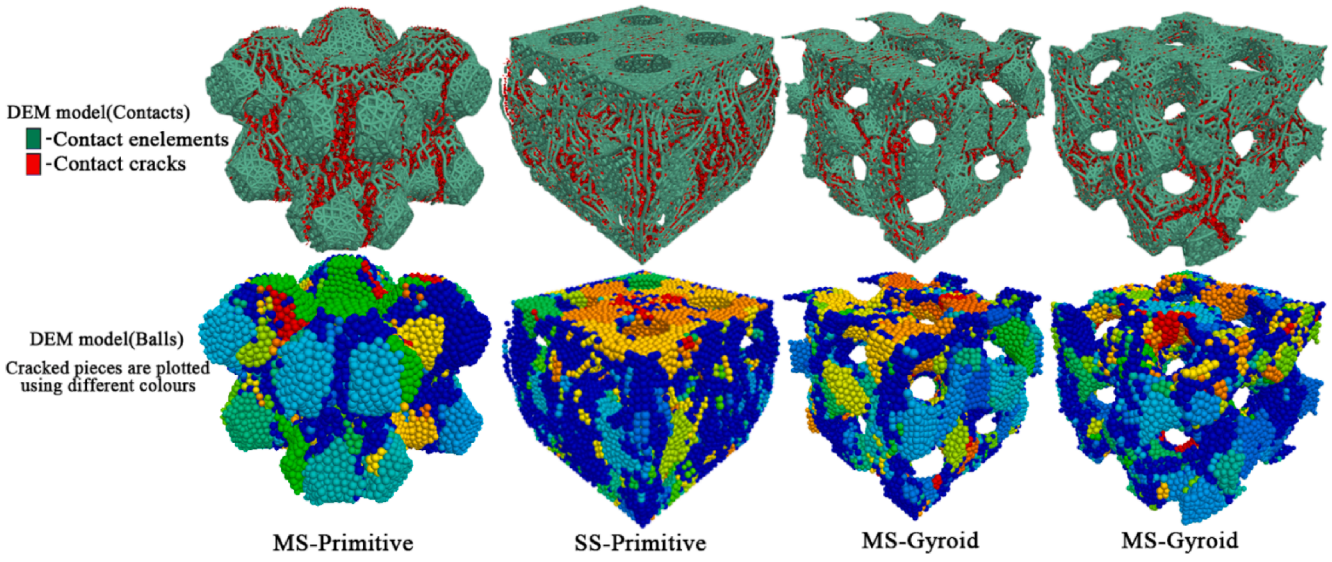

Fig. 11. The cracking patterns of the Gyroid and Primitive based structures under only compression.

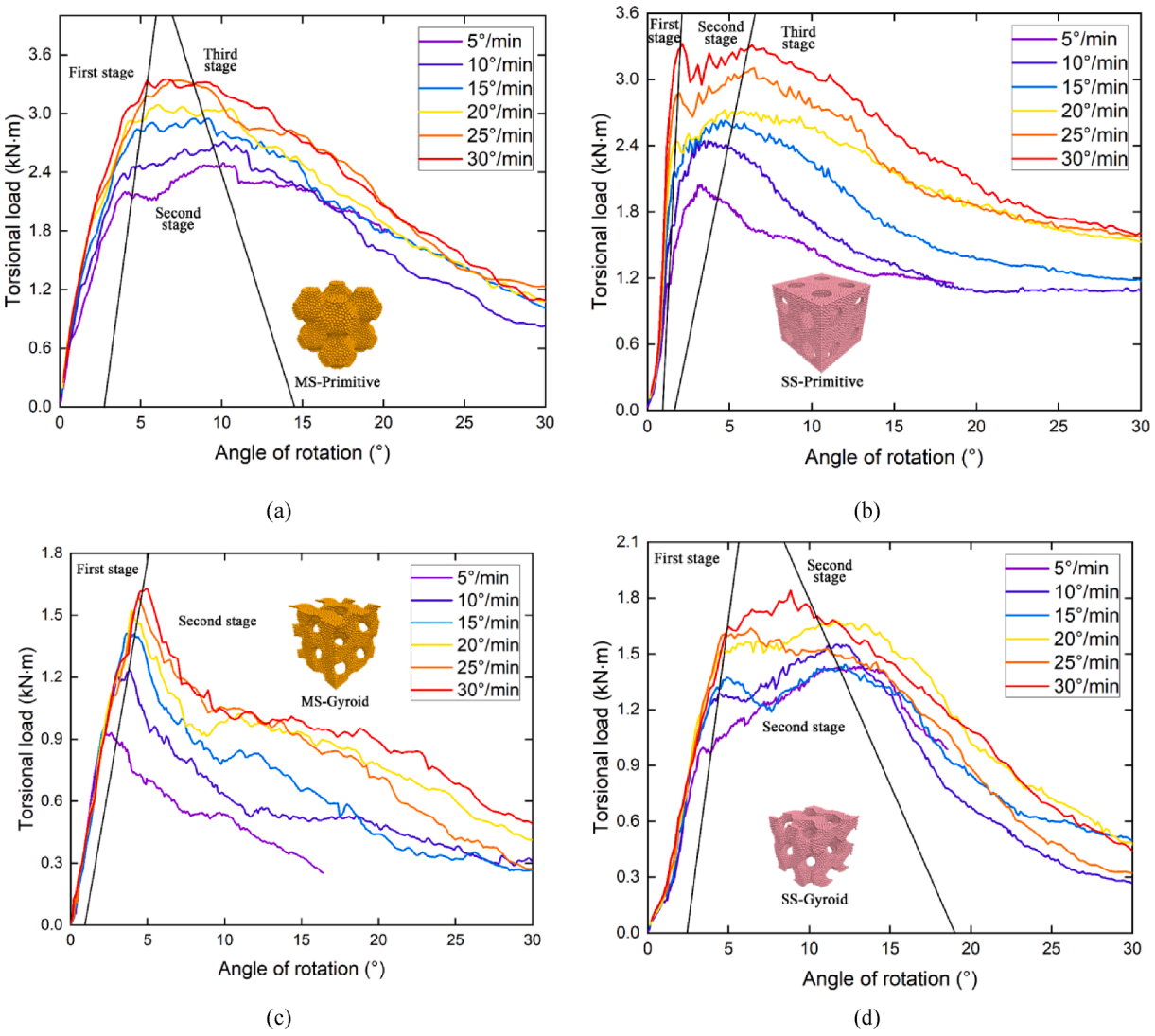

Fig. 12. The torsional load versus rotation angle of the top wall curves for (a) MS-Primitive, (b) SS-Primitive, (c) MS-Gyroid and (d) SS-Gyroid under torsional load only.

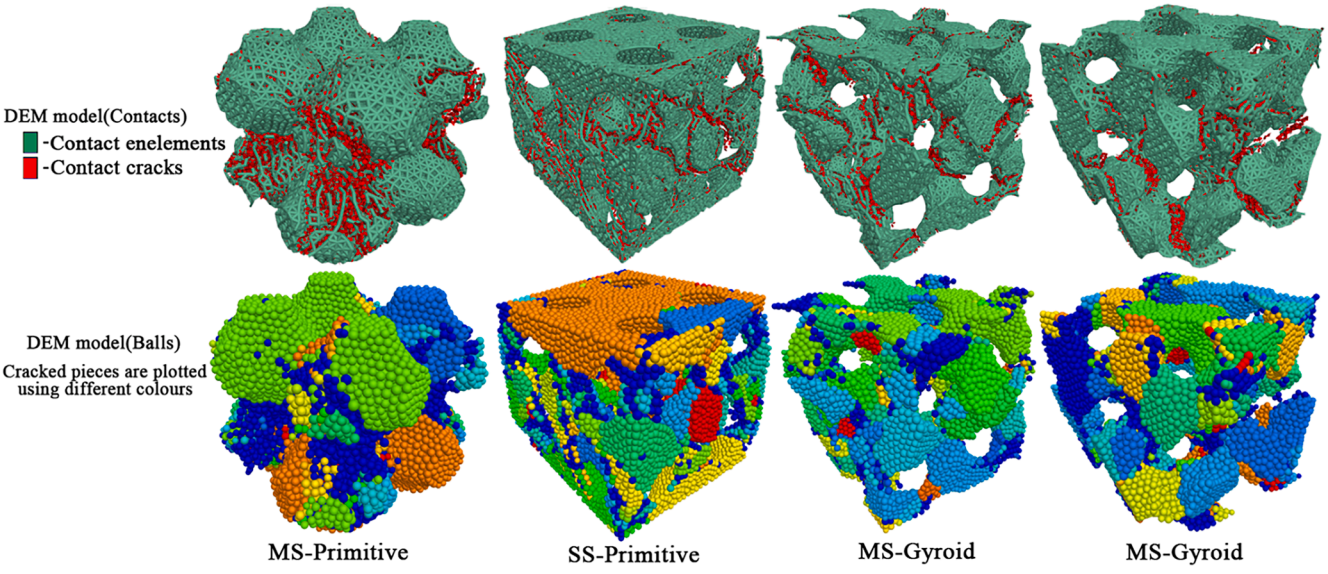

Fig. 13. The cracking patterns of the Gyroid and Primitive based structures under only torsional load at the spin rate of 20°/min.

maximum load in the first stage, and there is no significant plateau near the maximum torsional load. The difference in torsional behavior between the MS-Gyroid and SS-Gyroid structures may be attributed to their lack of axial symmetry. Although they share the same TPMS surface, the torsional direction can also affect their torsional behavior. The numerical simulation results indicate that Primitive structures exhibit better resistance to torsion than Gyroid structures at the same torsional loading rate, as demonstrated by their higher ultimate strength and improved ductility.

To examine the cracking patterns of the four TPMS structures under torsional loading only, the cracked DEM models after failure at a spin rate of 20°/min are compared in Fig. 13. It is found that the Primitive-based structures crack along the vertical direction, while the Gyroid-based structures crack along the transverse direction. The majority of cracks occur in the vertical bones inside the TPMS structures.

3.3. Behaviours of TPMS structures uder coupled compression and torsion load

In Fig. 14, the compressive load–displacement curves of the Primitive and Gyroid based structures under coupled compression and torsion loads at different torsional application rates are presented. It can be seen that the ultimate compressive load of all four TPMS structures decreases with an increase in the torsional application rate. At a spin rate of 25°/min, the TPMS structures almost attain their lowest compressive strength. The slope of the compressive load–displacement curve is an indicator of the compressive modulus of the structure. The numerical results show that the torsional rate has little effect on the compressive modulus in the linear stage. However, in the nonlinear stage, a higher torsional rate resulted in an earlier occurrence of the nonlinear stage and lower compressive stiffness. The ultimate compressive loads of MS-Primitive, SS-Primitive, MS-Gyroid and SS-Gyroid at a spin rate of 30°/min are 16.1 kN, 16.9 kN, 8.7 kN and 15.16 kN, accordingly. In comparison with the ultimate compressive loads under compressive load only, the values at 30°/min drop by 71.5%, 67.6%, 70.3% and 55.4%, respectively. These results suggest that TPMS structures can lose more than half of their compressive bearing capacity under combined compressive and torsional loads.

Fig. 15 compares the torsional load versus the rotation angle curves of the DEM simulation under coupled compressive and torsional loads at

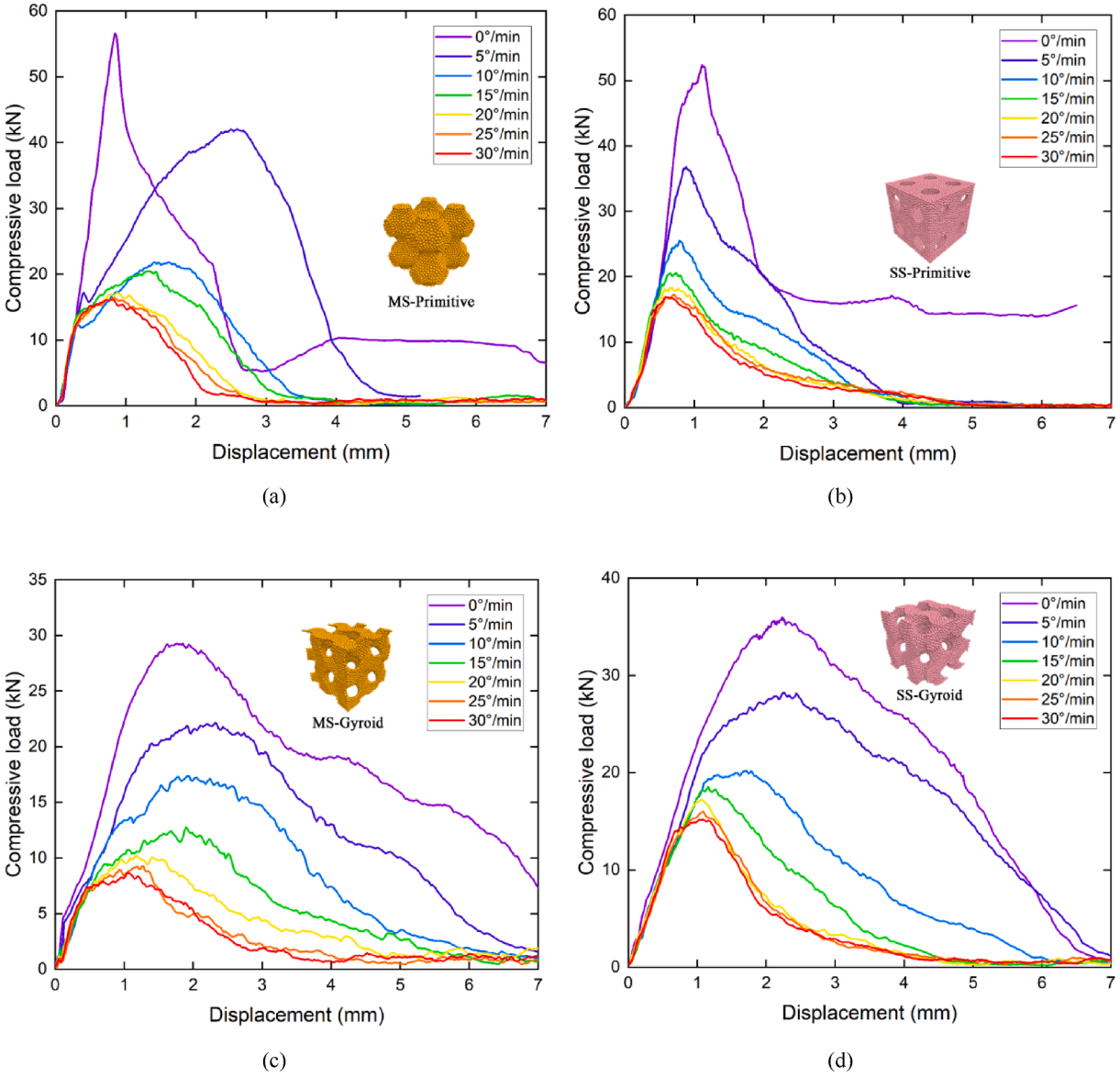

Fig. 14. The compressive load vesus displacement curves for (a) MS-Primitive, (b) SS-Primitive, (c) MS-Gyroid and (d) SS-Gyroid under coupled compressive and torsional loads.

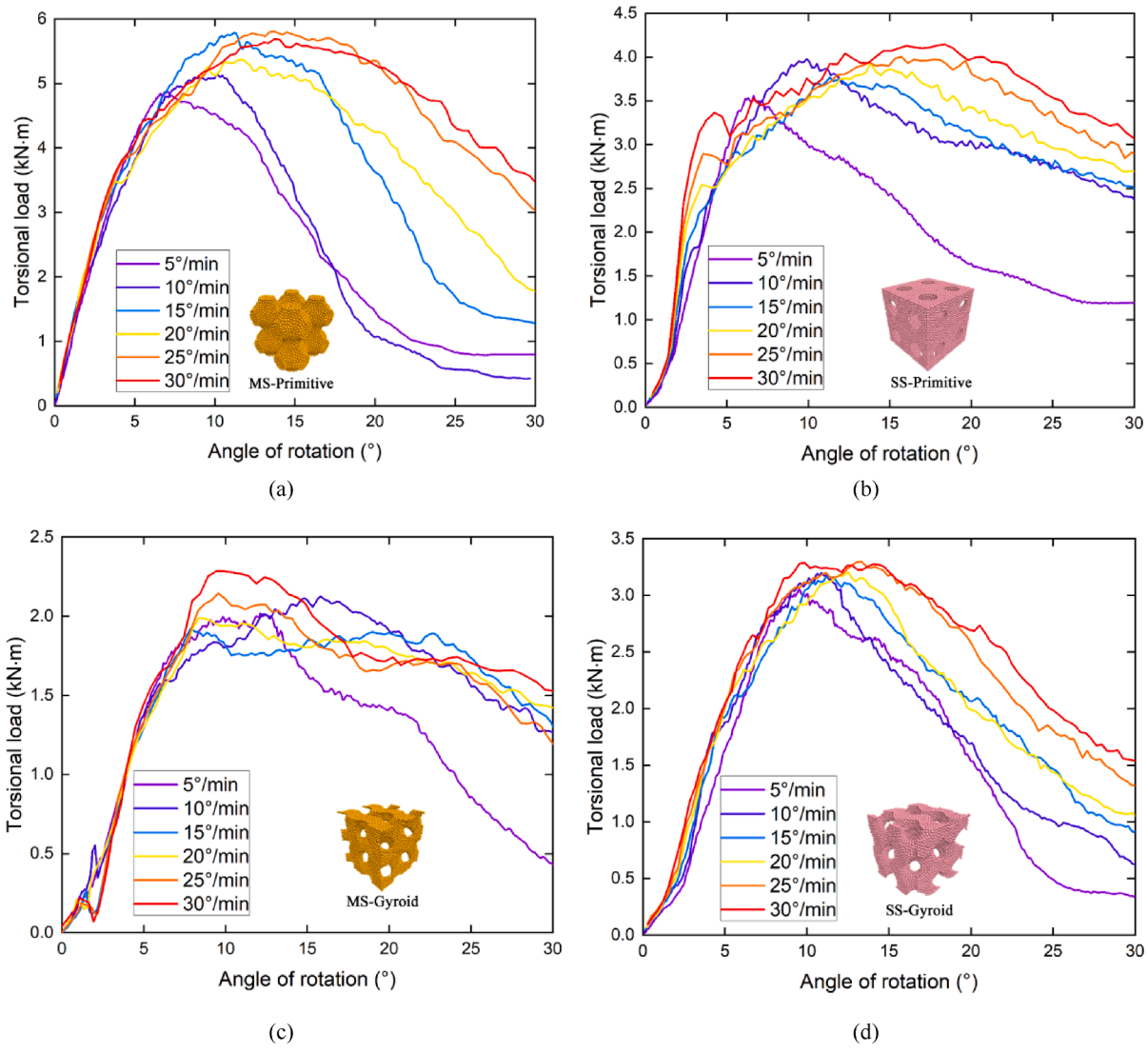

Fig. 15. The torsional load versus rotation angle curves for (a) MS-Primitive, (b) SS-Primitive, (c) MS-Gyroid and (d) SS-Gyroid under coupled compressive and torsional loads.

different spin rates. By comparing Fig. 15 with Fig. 12, it is evident that the torsional applying rate has a lesser impact on the ultimate torsional loads of the four TPMS structures under combined compression and torsion compared to under torsion only. A compressive load can significantly enhance the torsional bearing capacity of the Primitive and Gyroid based structures. Additionally, the four TPMS structures fail at higher rotation angles and exhibit greater residual torsional loads, which suggests that a compressive load can enhance the torsional ductility of the Primitive and Gyroid based structures. Under combined compression and torsion, Primitive-based structures exhibit higher torsional strength than Gyroid-based structures. Fig. 16 compares the ultimate compressive and torsional loads of the Primitive and Gyroid based structures under combined compressive and torsional loads It is clear that the Primitive based structures outperform the Gyroid based structures in both compression and torsion. Under the same loading conditions, the ultimate compressive and torsional loads of MS-Primitive and SS-Primitive structures are more than half higher than those of MS-Gyroid and SS-Gyroid structures. Fig. 17 compares the cracking patterns of the four TPMS structures under coupled compressive and torsional loads. By comparing Fig. 11, Fig. 13 and Fig. 17, it can be seen that the cracking areas of the four TPMS structures do not vary greatly. Primitive based structures primarily crack along the vertical and lateral directions, whereas Gyroid-based structures crack obliquely.

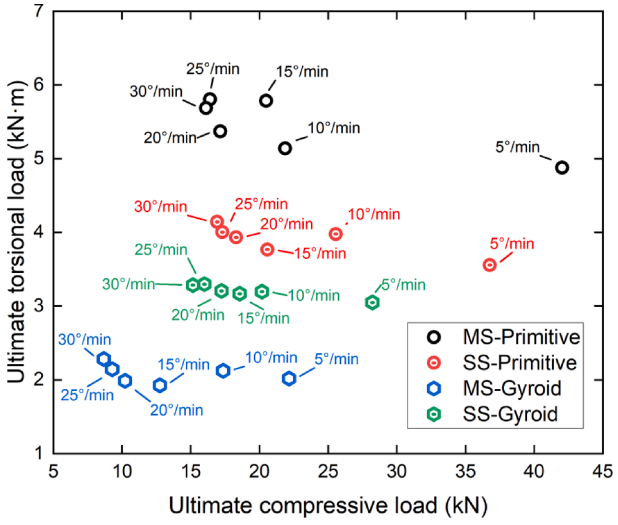

Fig. 16. Comparison of the ultimate compressive load and the ultimate torsional load of the MS-Primitive, the SS-Primitive, the MS-Gyroid and the SS-Gyroid structures when subject to coupled compressive and torsional loads.

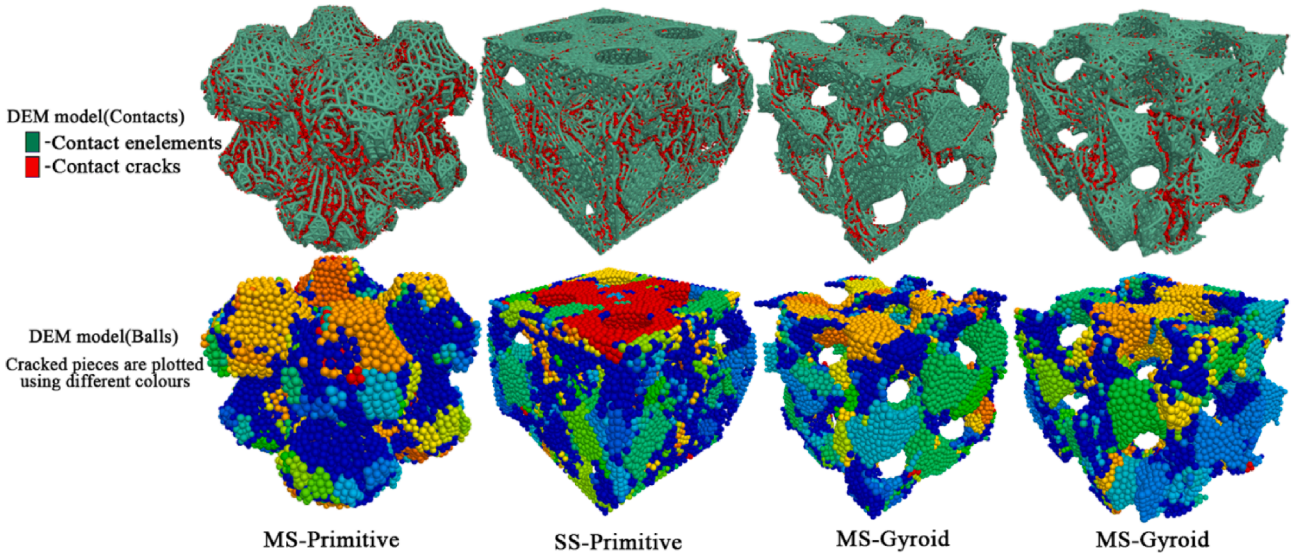

Fig. 17. The cracking patterns of the Gyroid and Primitive based structures under combined compression load and torsion load at the spin rate of 20°/min.

4. Conclusions

In this study, two representative TPMSs, the Gyroid surface and the Primitive surface, are employed to construct four TPMS blocks with a relative density of 0.5 and a size of $10 \times 10 \times 10$ cm^3. The discrete element method (DEM) is utilized to examine the mechanical behaviour of the MS-Primitive, SS-Primitive, MS-Gyroid, and SS-Gyroid structures when subjected to coupled compressive and torsional loads. A novel method for modelling concrete structures of complex shapes is proposed. Ball elements and nonlinear soft-bond contact elements are used to simulate the TPMS blocks. The compressive and torsional loads are applied using the motion and rotation of rigid wall elements. The material properties are based on experimental tests of concrete TPMS blocks, as reported in [53]. After verifying the DEM models through experimental compression tests, the models are subjected to combined compressive and torsional loads at varying loading rates. This study represents the first examination and comparison of the mechanical behaviour, including compressive bearing capacity, torsional bearing capacity, and cracking patterns, of concrete Primitive and Gyroid structures under combined torsion and compression. The key findings of the study include the following:

- The MS-Primitive and SS-Primitive structures exhibit superior compressive and torsional resistance compared to the MS-Gyroid and SS-Gyroid structures. The DEM results show that the Primitive-based structures have overall greater ultimate compressive and torsional loads than the Gyroid-based structures when subjected to the same load condition.
- Under combined compressive and torsional loads, the ultimate compressive loads of the four TPMS structures decrease rapidly with increasing torsion-applying rates. At a torsion rate of 30°/min, the compressive capacity of the structures is reduced by over 50% compared to only compressive load. In contrast, the ultimate torsional loads of the structures under combined torsion and compression are slightly improved compared to only torsional load.
- The loading conditions have limited impact on the cracking patterns of the four structures. The Primitive-based structures crack along vertical and lateral directions under both compression, torsion, and combined loads, while the Gyroid-based structures crack obliquely.

Triply periodic minimal surface (TPMS) structures have potential applications in the field of civil engineering due to their unique mechanical and architectural properties. TPMS structures have complex and repeating geometric patterns, which offer excellent stiffness and resistance to various loads, such as compression, tension, and torsion. These properties make TPMS structures ideal for use in a variety of potential civil engineering applications, including:

- Load-bearing structures: TPMS structures have been demonstrated to have superior compressive resistance, making them ideal for use in load-bearing structures, such as bridges and buildings.
- Energy-absorbing systems: TPMS structures have the ability to absorb and dissipate large amounts of energy, making them ideal for use in energy-absorbing systems, such as seismic dampers and shock absorbers.
- Noise barriers: TPMS structures have the potential to be used as noise barriers, as they have been demonstrated to reduce sound transmission and improve acoustics in laboratory tests.
- Decorative elements: The intricate and repeating patterns of TPMS structures can also be used as decorative elements in architectural designs, adding a unique and visually appealing aspect to structures.
- Light-weight construction: TPMS structures have a lightweight and efficient structure, making them ideal for use in light-weight construction and aerospace applications.

It is important to note that while TPMS structures have promising potential in these applications, further research and development are needed to fully understand and optimize their performance. The current work can help engineers to select a proper TPMS form for structures under combined compression and torsion loads.

CRediT authorship contribution statement

Hao Fu: Conceptualization, Methodology, Validation, Visualization, Formal analysis, Investigation, Writing – original draft, Writing – review & editing. **Junhui Huang:** Conceptualization, Software, Visualization, Formal analysis, Investigation, Writing – original draft, Writing – review & editing. **Sakdirat Kaewunruen:** Conceptualization, Formal analysis, Investigation, Writing – review & editing, Supervision, Project administration, Funding acquisition.

Declaration of Competing Interest

The authors declare that they have no known competing financial interests or personal relationships that could have appeared to influence the work reported in this paper.

Data availability

Data will be made available on request.

Acknowledgements:

The first author has received the PhD scholarship from China Scholarship Council. The research was funded by the European Commission for Shift2Rail S-Code Project (Grant No. 730849) and H2020-MSCA-RISE Project No. 691135 "RISEN: Rail Infrastructure Systems Engineering Network," which enables a global research network that tackles the grand challenge in railway infrastructure resilience and advanced sensing under extreme conditions. The APC is funded by the University of Birmingham Library's Open Access Fund.

References

[1] Herzog D, Seyda V, Wycisk E, Emmelmann C. Additive manufacturing of metals. Acta Mater 2016;117:371–92.
[2] Gao W, Zhang Y, Ramanujan D, Ramani K, Chen Y, Williams CB, et al. The status, challenges, and future of additive manufacturing in engineering. Comput Aided Des 2015;69:65–89.
[3] Braga DFO, Tavares SMO, da Silva LFM, Moreira PMGP, de Castro PMST. Advanced design for lightweight structures: Review and prospects. Prog Aerosp Sci 2014;69:29–39.
[4] Plocher J, Panesar A. Review on design and structural optimisation in additive manufacturing: Towards next-generation lightweight structures. Mater Des 2019;183:108164.
[5] Limmahakhun S, Oloyede A, Sitthiseripratip K, Xiao Y, Yan C. 3D-printed cellular structures for bone biomimetic implants. Addit Manuf 2017;15:93–101.
[6] Gopinathan J, Noh I. Recent trends in bioinks for 3D printing. Biomaterials Research 2018;22:11.
[7] Opgenoord MMJ, Willcox KE. Design for additive manufacturing: cellular structures in early-stage aerospace design. Struct Multidiscip Optim 2019;60:411–28.
[8] Hohe J, Hardenacke V, Fascio V, Girard Y, Baumeister J, Stöbener K, et al. Numerical and experimental design of graded cellular sandwich cores for multi-functional aerospace applications. Mater Des 2012;39:20–32.
[9] Jenett B, Abdel-Rahman A, Cheung K, Gershenfeld N. Material-Robot System for Assembly of Discrete Cellular Structures. IEEE Rob Autom Lett 2019;4:4019–26.
[10] Maurath J, Willenbacher N. 3D printing of open-porous cellular ceramics with high specific strength. J Eur Ceram Soc 2017;37:4833–42.
[11] Hu Z, Thiyagarajan K, Bhusal A, Letcher T, Fan QH, Liu Q, et al. Design of ultra-lightweight and high-strength cellular structural composites inspired by biomimetics. Compos B Eng 2017;121:108–21.
[12] Jin Q-Y, Yu J-H, Ha K-S, Lee W-J, Park S-H. Multi-dimensional lattices design for ultrahigh specific strength metallic structure in additive manufacturing. Mater Des 2021;201:109479.
[13] Challis VJ, Xu X, Zhang LC, Roberts AP, Grotowski JF, Sercombe TB. High specific strength and stiffness structures produced using selective laser melting. Mater Des 2014;63:783–8.
[14] Li D, Liao W, Dai N, Xie YM. Comparison of Mechanical Properties and Energy Absorption of Sheet-Based and Strut-Based Gyroid Cellular Structures with Graded Densities. Materials 2019.
[15] Fu H, Kaewunruen S. Experimental and DEM investigation of axially-loaded behaviours of IWP-based structures. Int J Mech Sci 2022;235:107738.
[16] Gibson LJ. Biomechanics of cellular solids. J Biomech 2005;38:377–99.
[17] Yuan L, Ding S, Wen C. Additive manufacturing technology for porous metal implant applications and triple minimal surface structures: A review. Bioact Mater 2019;4:56–70.
[18] Yin H, Zhang W, Zhu L, Meng F, Liu J, Wen G. Review on lattice structures for energy absorption properties. Compos Struct 2023;304:116397.
[19] Fu H, Kaewunruen S. State-of-the-Art Review on Additive Manufacturing Technology in Railway Infrastructure Systems. Journal of Composites. Science 2022.
[20] Werner JG, Rodríguez-Calero GG, Abruña HD, Wiesner U. Block copolymer derived 3-D interpenetrating multifunctional gyroidal nanohybrids for electrical energy storage. Energ Environ Sci 2018;11:1261–70.
[21] Tran P, Peng C. Triply periodic minimal surfaces sandwich structures subjected to shock impact. J Sandw Struct Mater 2020;23:2146–75.
[22] Sharma D, Hiremath SS. Additively manufactured mechanical metamaterials based on triply periodic minimal surfaces: Performance, challenges, and application. Mech Adv Mater Struct 2021;1–31.
[23] Saranathan V, Osuji CO, Mochrie SG, Noh H, Narayanan S, Sandy A, et al. Structure, function, and self-assembly of single network gyroid (I4132) photonic crystals in butterfly wing scales. Proc Natl Acad Sci U S A 2010;107:11676–81.
[24] Novak N, Al-Ketan O, Krstulović-Opara L, Rowshan R, Abu Al-Rub RK, Vesenjak M, et al. Quasi-static and dynamic compressive behaviour of sheet TPMS cellular structures. Compos Struct 2021;266:113801.
[25] Monkova K, Vasina M, Zaludek M, Monka PP, Tkac J. Mechanical Vibration Damping and Compression Properties of a Lattice Structure. Materials 2021;14.
[26] Maskery I, Sturm L, Aremu AO, Panesar A, Williams CB, Tuck CJ, et al. Insights into the mechanical properties of several triply periodic minimal surface lattice structures made by polymer additive manufacturing. Polymer 2018;152:62–71.
[27] Lee D-W, Khan KA, Abu Al-Rub RK. Stiffness and yield strength of architectured foams based on the Schwarz Primitive triply periodic minimal surface. Int J Plast 2017;95:1–20.
[28] Lai M, Kulak AN, Law D, Zhang Z, Meldrum FC, Riley DJ. Profiting from nature: macroporous copper with superior mechanical properties. Chem Commun (Camb) 2007;3547–9.
[29] Khan SZ, Masood SH, Ibrahim E, Ahmad Z. Compressive behaviour of Neovius Triply Periodic Minimal Surface cellular structure manufactured by fused deposition modelling. Virtual and Physical Prototyping 2019;14:360–70.
[30] Kapfer SC, Hyde ST, Mecke K, Arns CH, Schröder-Turk GE. Minimal surface scaffold designs for tissue engineering. Biomaterials 2011;32:6875–82.
[31] Han L, Che S. An Overview of Materials with Triply Periodic Minimal Surfaces and Related Geometry: From Biological Structures to Self-Assembled Systems. Adv Mater 2018;30:1705708.
[32] De Oliveira AR, De Andrade Mendes Filho A, Masoumi M, Del Conte EG. Compression and energy absorption of maraging steel primitive scaffolds produced by powder bed fusion. The International Journal of Advanced Manufacturing Technology. 2021;116:1271-83.
[33] Al-Ketan O, Soliman A, AlQubaisi AM, Abu Al-Rub RK. Nature-Inspired Lightweight Cellular Co-Continuous Composites with Architected Periodic Gyroidal Structures. Adv Eng Mater 2018;20:1700549.
[34] Al-Ketan O, Rowshan R, Palazotto AN, Abu Al-Rub RK. On Mechanical Properties of Cellular Steel Solids With Shell-Like Periodic Architectures Fabricated by Selective Laser Sintering. J Eng Mater Technol 2019;141.
[35] Al-Ketan O, Adel Assad M, Abu Al-Rub RK. Mechanical properties of periodic interpenetrating phase composites with novel architected microstructures. Compos Struct 2017;176:9–19.
[36] Abueidda DW, Elhebeary M, Shiang C-S, Pang S, Abu Al-Rub RK, Jasiuk IM. Mechanical properties of 3D printed polymeric Gyroid cellular structures: Experimental and finite element study. Mater Des 2019;165:107597.
[37] Abueidda DW, Bakir M, Abu Al-Rub RK, Bergström JS, Sobh NA, Jasiuk I. Mechanical properties of 3D printed polymeric cellular materials with triply periodic minimal surface architectures. Mater Des 2017;122:255–67.
[38] Abueidda DW, Abu Al-Rub RK, Dalaq AS, Younes HA, Al Ghaferi AA, Shah TK. Electrical conductivity of 3D periodic architectured interpenetrating phase composites with carbon nanostructured-epoxy reinforcements. Compos Sci Technol 2015;118:127–34.
[39] Abueidda DW, Abu Al-Rub RK, Dalaq AS, Lee D-W, Khan KA, Jasiuk I. Effective conductivities and elastic moduli of novel foams with triply periodic minimal surfaces. Mech Mater 2016;95:102–15.
[40] Zhang Y, Hsieh M-T, Valdevit L. Mechanical performance of 3D printed interpenetrating phase composites with spinodal topologies. Compos Struct 2021;263:113693.
[41] Jiang D, Ning F. Physical-mechanical behaviors of stainless steel plate-lattice built by material extrusion additive manufacturing. J Mater Process Technol 2022;309:117739.
[42] Briels D, Kollmannsberger S, Leithner F, Matthäus C, Nouman AS, Oztoprak O, et al. Thermal Optimization of Additively Manufactured Lightweight Concrete Wall Elements with Internal Cellular Structure through Simulations and Measurements. Buildings 2022.
[43] Ghanbari-Ghazijahani T, Kasebahadi M, Hassanli R, Classen M. 3D printed honeycomb cellular beams made of composite materials (plastic and timber). Constr Build Mater 2022;315:125541.
[44] Du W, Zhu L, Zhang H, Zhou Z, Wang K, Uddin N. Experimental and Numerical Investigation of an Innovative 3DPC Thin-Shell Structure. Buildings 2023.
[45] Bello ND, Memari AM. Comparative Review of the Technology and Case Studies of 3D Concrete Printing of Buildings by Several Companies. Buildings 2023.
[46] Ahamed MK, Wang H, Hazell PJ. From biology to biomimicry: Using nature to build better structures – A review. Constr Build Mater 2022;320:126195.
[47] Zhang J, Wang J, Dong S, Yu X, Han B. A review of the current progress and application of 3D printed concrete. Compos A Appl Sci Manuf 2019;125:105533.
[48] Siddika A, Mamun MAA, Ferdous W, Saha AK, Alyousef R. 3D-printed concrete: applications, performance, and challenges. J Sustain Cement-Based Mater 2020;9:127–64.
[49] Salet TAM, Ahmed ZY, Bos FP, Laagland HLM. Design of a 3D printed concrete bridge by testing. Virtual Phys Prototyping 2018;13:222–36.
[50] Nodehi M, Aguayo F, Nodehi SE, Gholampour A, Ozbakkaloglu T, Gencel O. Durability properties of 3D printed concrete (3DPC). Autom Constr 2022;142:104479.
[51] Hou S, Duan Z, Xiao J, Ye J. A review of 3D printed concrete: Performance requirements, testing measurements and mix design. Constr Build Mater 2021;273:121745.
[52] Khoshnevis B. Automated construction by contour crafting—related robotics and information technologies. Autom Constr 2004;13:5–19.
[53] Nguyen-Van V, Tran P, Peng C, Pham L, Zhang G, Nguyen-Xuan H. Bioinspired cellular cementitious structures for prefabricated construction: Hybrid design & performance evaluations. Autom Constr 2020;119:103324.
[54] Nguyen-Van V, Panda B, Zhang G, Nguyen-Xuan H, Tran P. Digital design computing and modelling for 3-D concrete printing. Autom Constr 2021;123:103529.
[55] Nguyen-Van V, Liu J, Peng C, Zhang G, Nguyen-Xuan H, Tran P. Dynamic responses of bioinspired plastic-reinforced cementitious beams. Cem Concr Compos 2022;133:104682.

[56] Nguyen-Van V, Choudhry NK, Panda B, Nguyen-Xuan H, Tran P. Performance of concrete beam reinforced with 3D printed Bioinspired primitive scaffold subjected to three-point bending. Autom Constr 2022;134:104060.
[57] Karakoç A. RegionTPMS — Region based triply periodic minimal surfaces (TPMS) for 3-D printed multiphase bone scaffolds with exact porosity values. SoftwareX 2021;16:100835.
[58] Sengsri P, Fu H, Kaewunruen S. Mechanical Properties and Energy-Absorption Capability of a 3D-Printed TPMS Sandwich Lattice Model for Meta-Functional Composite Bridge Bearing Applications. Journal of Composites. Science 2022.
[59] Gutiérrez-Ch JG, Senent S, Melentijevic S, Jimenez R. Distinct element method simulations of rock-concrete interfaces under different boundary conditions. Eng Geol 2018;240:123–39.
[60] Zhai M, Xue L, Bu F, Yang B, Ding H. Microcracking behaviors and acoustic emission characteristics of granite subjected to direct shear based on a novel grain-based model. Comput Geotech 2022;151:104955.
[61] Brown NJ, Chen J-F, Ooi JY. A bond model for DEM simulation of cementitious materials and deformable structures. Granul Matter 2014;16:299–311.
[62] Hentz S, Daudeville L, Donzé FV. Identification and Validation of a Discrete Element Model for Concrete. J Eng Mech 2004;130:709–19.